Numerical Analysis of Store-Induced Limit-Cycle Oscillation

P. S. Beran,[*] N. S. Khot,[†] F. E. Eastep,[‡] R. D. Snyder,[§] and J. V. Zweber[¶]
U.S. Air Force Research Laboratory, Wright–Patterson Air Force Base, Ohio 45433

Store-induced limit-cycle oscillation of a rectangular wing with tip store in transonic flow is simulated using a variety of mathematical models for the flowfield: transonic small-disturbance theory (with and without inclusion of store aerodynamics) and transonic small-disturbance theory with interactive boundary layer (without inclusion of store aerodynamics). For the conditions investigated, assuming inviscid flow, limit-cycle oscillations are observed to occur as a result of a weakly subcritical Hopf bifurcation and are obtained at speeds lower than those predicted 1) nonlinearly for clean-wing flutter and 2) linearly for wing/store flutter. The ability of transonic small-disturbance theory to predict the occurrence and strength of this type of limit-cycle oscillation is compared for the different models. Differences in unmatched and matched aeroelastic analysis are described. Solutions computed for the clean rectangular wing are compared to those computed with the Euler equations for a case of static aeroelastic behavior and for a case of forced, rigid-wing oscillation at Mach 0.92.

Nomenclature

C_L, C_M	=	lift and moment coefficients (moment about leading edge)
c	=	chord, ft
c.g., ea	=	center of gravity and elastic axis, ft from leading edge
i, j, k	=	computational index coordinates
l	=	span, ft
M	=	Mach number
Re	=	Reynolds number (based on root chord)
T	=	temperature, °R
t	=	time, s
U	=	velocity, ft/s
x, y, z	=	physical coordinates (streamwise, spanwise, vertical), ft
α	=	angle of attack, deg
ζ	=	structural damping coefficient, nondimensional
ρ	=	density, slugs/ft³

Subscripts

s, w	=	store or wing property, respectively
0	=	wing root property
∞	=	freestream condition

Introduction

HIGH-PERFORMANCE fighter aircraft with external stores are required to operate with high maneuverability in the transonic flight regime. In this regime, the potential exists for encountering transonic nonlinear flutter, known as limit-cycle oscillation (LCO). LCO is a limited-amplitude, self-sustaining oscillation produced by an aerodynamic-structural interaction, which for the cases of interest is exasperated by the occurrence of shock waves on the surface of the wing and/or stores. LCO results in an undesirable airframe vibration and limits the performance of the flight vehicle.

The main goal of the current work is to determine the range of applicability of models of varying fidelity to the numerical prediction of store-induced LCO. This form of LCO typically occurs near linear flutter boundaries in the nonlinear, transonic regime (Mach number ranging between 0.8 and 1.1), suggesting that classical flutter predictions using linear aerodynamic theories can be applied to the identification of lightly damped modes that can nonlinearly participate in LCO. Indeed, using traditional approaches, Denegri[1] had limited success in relating observed store-induced LCO to "hump" (or "soft" crossing) modes found in velocity-damping diagrams.

Previous work has typically focused on the effects of stores on wing flutter speeds, or on the influence of static nonlinearities on wing flutter speeds. For example, Turner[2] investigated the aerodynamic influence of stores on four different fighter aircraft. This detailed study was limited to linear aerodynamic theory, as implemented within MSC/NASTRAN using a nonplanar doublet-lattice method and slender body theory. In another thorough investigation, Gern and Librescu[3] investigated the static and dynamic behaviors of swept wings with external stores. Although the structural modeling was comprehensive, linear aerodynamics based on strip theory was employed to model the flight loads. Eastep and Olsen[4] examined the impact of static aerodynamic nonlinearities on the behavior of the flutter boundary for a clean wing in the transonic regime.

However, in cases of interest involving LCO the assumption of linear/linearized aerodynamics prevents the capture of the proper flowfield physics. The transonic regime differs from the linear, subsonic regime by the appearance of shocks. These structures can strongly interact with vehicle boundary layers, with the possible consequences of flow separation or significant shock movement. Linear aerodynamic theories do not capture these behaviors, nor do linearized theories properly represent dynamic nonlinearities arising from shock movement, or time-dependent interaction between the shock and boundary layer. Fundamentally, the saturation of LCO amplitudes (but not necessarily the loss of stability to LCO) is a dynamically nonlinear process, which cannot be modeled by a linearized approach.

Following advances in nonlinear modeling and computer hardware, nonlinear aeroelastic predictions, including viscous effects and maneuver loads, are tractable for reasonably complex configurations.[5−7] Still, the use of modeling techniques that account for viscosity is too computationally demanding for preliminary design. In a coordinated manner, we examine the ability of aeroelastic models of varying fidelity to predict accurately LCO onset and amplitude. Models based on linear analysis, transonic small-disturbance theory (TSDT), and TSDT with interactive boundary

*Principal Research Aerospace Engineer, AFRL/VASD, Building 146, 2210 8th Street; philip.beran@wpafb.af.mil. Associate Fellow AIAA.

†Principal Research Aerospace Engineer, AFRL/VASD. Associate Fellow AIAA.

‡NRC Senior Research Associate, AFRL/VASD; franklin.eastep@wpafb.af.mil. Fellow AIAA.

§Aerospace Engineer, AFRL/VASD; richard.snyder@wpafb.af.mil. Senior Member AIAA.

¶Aerospace Engineer, AFRL/VASD; jeffrey.zweber@wpafb.af.mil. Senior Member AIAA.

layer are considered. Through this approach, we discern 1) the limitations of linear theory for LCO prediction vis a vis the simplest nonlinear theory capable of producing weak shocks; 2) the ability of TSDT to predict store-induced LCO in inviscid flow; and 3) the effects of viscosity on store-induced LCO. This work provides the increased understanding of the LCO phenomenon, while also serving to determine the range of applicability and computational cost of various modeling techniques to the prediction of this phenomenon.

Three computational methodologies are employed in this investigation: the MSC/NASTRAN aeroelastic analysis program, the TSDT-based NASA/LaRC CAPTSDv computational aeroelasticity algorithm for inviscid and viscous flow, and the U.S. Air Force Research Laboratory ENS3DAE Euler/Navier–Stokes computational aeroelasticity algorithm. MSC/NASTRAN is used in the development and analysis of structural models, the prediction of linear aeroelastic response of selected wing/store configurations, and the search for configurations speculated herein to produce LCO. The CAPTSDv algorithm is used to carry out relatively fast aeroelastic analyses for inviscid flow and viscous flow through interactive boundary-layer coupling, starting with cases previously identified by MSC/NASTRAN as LCO susceptible. ENS3DAE is then applied to validate CAPTSDv predictions for static aeroelastic and dynamic rigid behavior for a representative set of flow conditions.

Problem Formulation

The wing studied herein is derived from the "heavy" version of the original Goland wing. Like the original, the heavy wing is structurally represented by a beam, but with additional nonstructural mass, as defined by Eastep and Olsen.[4] This latest version, referred to as the Goland$^+$ wing, is a heavy wing modeled with a box structure to enable a variety of store attachment options.

Geometry and Structure

The Goland$^+$ wing is rectangular and cantilevered from an infinite midplane (Fig. 1a). In this study, the following values of geometric parameters are assumed: $c_w = 6$, $l_w = 20$, $c_s = 10$, and $l_s = 1$. The airfoil section is assumed to be constant over the spanwise extent of the wing and is chosen to be that of a symmetric, 4%-thick, parabolic-arc airfoil, defined by $z = \pm 0.08x(1 - x/c_w)$ for $0 \leq x \leq c_w$. The wing-tip store is mounted flush to the wing tip (Fig. 1a). The sectional shape of the store is also described by a parabolic arc, uniform in the spanwise direction, and with a thickness 50% greater than that of the wing. The leading edge of the store is offset (defined positive; $c_{off} = 3$) upstream of the wing leading edge, thereby providing the shape formula $z = \pm 0.072(x + c_{off})[1 - (x + c_{off})/c_s]$ for $-c_{off} \leq x \leq c_s - c_{off}$.

The wing-box structure finite element model is built up from shear panels, modeling the spars and ribs, and membrane elements, modeling the wing skins. In addition, rod elements are included to model spar and rib caps as well as posts that connect the wing skins at every spar/rib intersection. Every element is modeled using a Young's modulus of 1.4976×10^9 slugs/ft^2, a shear modulus of 5.616×10^8 slugs/ft^2, and a structural density of 0.0001 slugs/ft^3. The model was built with a very low structural density to allow the stiffness and mass properties to be decoupled. This decoupling allows the elements to be sized to tune the model to match the structural dynamic characteristics of the beam model of the heavy Goland wing.

The geometry of the wing box is simple. The origin is at the midheight of the root of the leading-edge spar. The three spars are unswept and placed at 0, 2, and 4 ft along the positive x coordinate. The 11 ribs are evenly spaced on 2-ft centers along the positive y coordinate. The shear elements are defined by the intersections of the
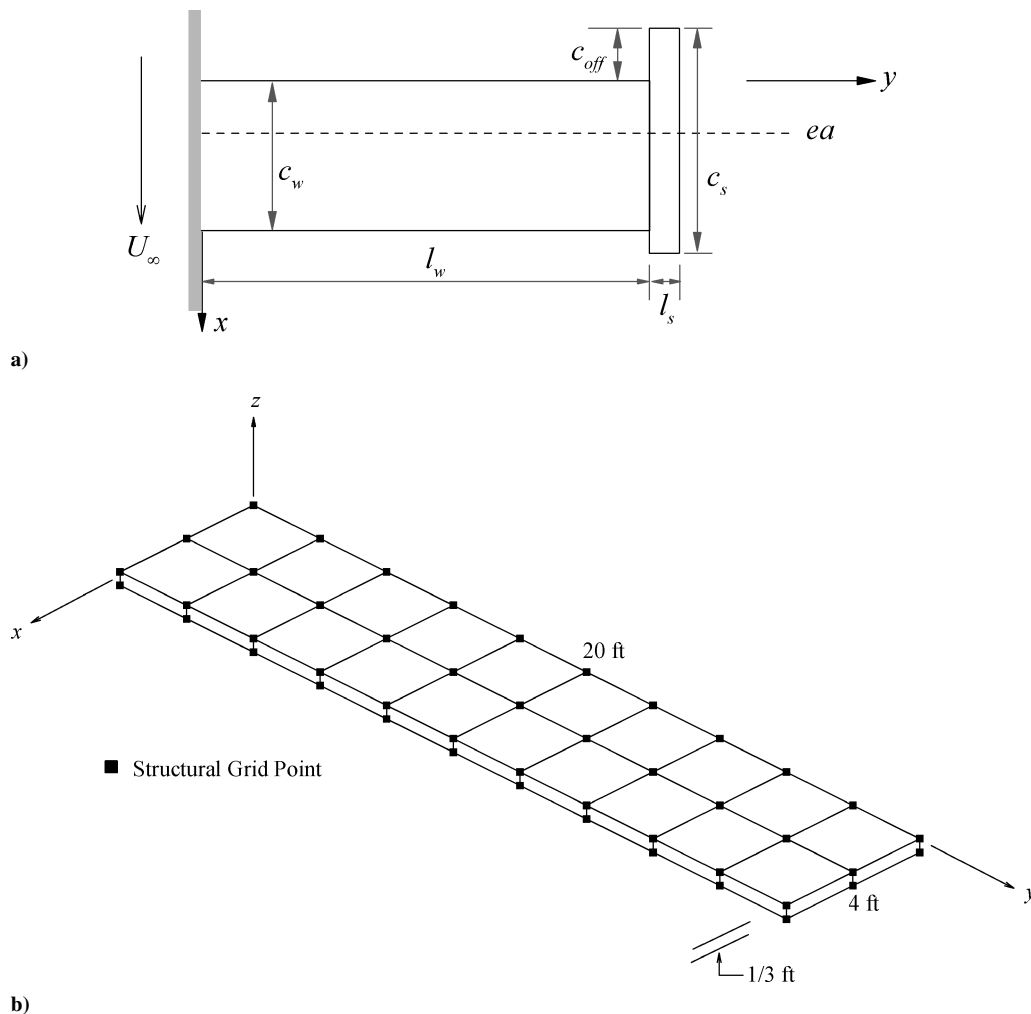

Fig. 1   Schematics of Goland$^+$ wing geometry and structural model: a) planform geometry and b) structural model.

spars and ribs, with 10 elements per spar and two elements per rib. Next, each spar and rib is 0.33334 ft high, and each cell defined by the spars and ribs is capped with a single wing skin membrane element. This results in a total of 40 skin elements. Finally, rods are added on the top and bottom of each shear element and at every spar/rib intersection. The total number of rod elements is 137, consisting of 60 spar caps, 44 rib caps, and 33 posts.

The mass properties of this wing are modeled by placing lumped masses with no rotational inertia at each grid point. The lumped masses are sized to match the mass properties (total mass, c.g., and inertia) of the heavy Goland wing. For the beam model Goland wing, the mass properties are simply modeled as lumped mass with rotational inertia centered at the c.g. of sections placed at 2-ft intervals. For the internal rib locations of the (i.e., 2 ft, 4 ft, 6 ft, etc.) beam model, the lumped mass properties were a mass of 22.496 slugs, with a rotational inertia in pitch of 50.3396 slug-ft^2, centered at $x = 2.6$ ft. For the external rib locations (i.e., 0 and 20 ft), the lumped mass properties were halved. In the built-up wing model, the masses used for the internal rib locations are as follows: 1.9650 slugs at each leading-edge point, 3.9442 slugs at each point on the center spar, and 5.3398 slugs for the trailing-edge points. Also, similar to the beam model, the masses used at the external spar locations are half of the amount used at the internal locations.

The final step in developing the built-up model is sizing the elements so that its structural dynamic characteristics match those of the beam model Goland wing. For this model development, the elements are sized to minimize the error between the first three frequencies of the built-up and beam models. The boundary condition for each model is cantilevered. To maintain symmetry, the elements are grouped by their component. The thicknesses (in feet) for the two-dimensional elements are upper and lower wing skins—0.0155; leading- and trailing-edge spar—0.0006; center spar—0.0889; and rib—0.0347. For the one-dimensional elements, the areas (in ft^2) are posts—0.0008; leading- and trailing-edge spar caps—0.0416; center spar cap—0.1496; and rib cap—0.0422.

The store configuration examined in this work is that of a tip store. This store structure is modeled as a series of rigid bar elements that result in a 10-ft-long rigid bar. The resultant bar is centered 0.5 ft outboard of the wing tip and 2 ft aft of the wing leading edge. The store is then rigidly connected to the six wing-tip grid points. This is accomplished by defining a seventh wing-tip grid point at the center of the rib structural model (i.e., $x = 2$ ft, $y = 20$ ft, $z = 0$ ft) and connecting this point to the other six points with a MSC/NASTRAN RBE3 element. This results in the displacement of the seventh grid point being the average of the displacements of the original six points. Finally, an RBAR element is used to connect the seventh wing-tip point to the corresponding point (i.e., $x = 2$ ft, $y = 20.5$ ft, $z = 0$ ft) of the tip store model.

The mass properties of the tip store are chosen to match the properties of one section of the wing: a mass of 22.496 slugs and a rotational inertia of 50.3396 slug-ft^2. During this study, the position of the store mass is fixed at the lateral and vertical centers of the store (i.e., $y = 20.5$ ft and $z = 0$ ft) and varied in the streamwise direction.

Computational Aeroelasticity Methods

CAPTSD solves the three-dimensional, transonic, small-disturbance, potential-flow equations for partial and complete aircraft configurations.[8,9] The standard, most widely distributed version of the program computes inviscid, compressible flow for combinations of wings, fuselage, horizontal tail, bodies/stores, and rectangular planform vertical surfaces. CAPTSD solves the aerodynamic equations of motion using a time-accurate algorithm that is capable of simulating both steady and unsteady flow.[10] The method is capable of computing aeroelastic interactions by coupling the aerodynamic module with a structural dynamics simulation. The structural dynamics of horizontal surfaces are simulated in CAPTSD by using a modal structural model. The structural analysis is coupled to the aerodynamic analysis by a process that transfers generalized aerodynamic forces and generalized displacements between the aerodynamics and structural dynamics modules. Using this approach,

CAPTSD is capable of simulating both static and dynamic aeroelastic phenomena.

A viscous-inviscid interaction version of CAPTSD, known as CAPTSDv, has been developed[11,12] and applied to a variety of problems involving mildly separated and separation onset flows.[13] The method couples the inviscid CAPTSD algorithm with an inverse integral boundary-layer model. The boundary-layer equations are solved in a quasi-steady formulation similar to that recommended by Green et al.[14] The outer inviscid solution and the inner viscous solution are computed independently and are coupled using an active control mechanism that minimizes coupling errors for unsteady flows. In this investigation, a single version of the CAPTSDv algorithm is used to perform both inviscid and viscous aeroelastic analysis (execution mode controlled by user).

CAPTSD solves the equations of motion on a sheared Cartesian grid system where lifting surfaces are modeled as thin plates. Thickness and camber information for the upper and lower surfaces of each lifting surface is supplied through a set of surface slopes that are specified as boundary conditions for the algorithm. Similarly, structural mode shapes are supplied as surface slope perturbations. This approach greatly simplifies the modeling task required for an aeroelastic analysis because the grids are typically simple to generate and no moving grid algorithm is required for the aeroelastic simulation. CAPTSD is 1–1.5 orders of magnitude more computationally efficient than higher-fidelity methods and offers the potential for nonlinear aerodynamics analysis within a design framework using the CAPTSD methodology.

Aeroelastic analysis of the Euler and Navier–Stokes equations is carried out with the Euler/Navier–Stokes three-dimensional aeroelastic (ENS3DAE) method. The Lockheed–Georgia Company, under contract to the Air Force Wright Laboratory, developed ENS3DAE in the late 1980s (Ref. 15). This program has been used to solve numerous aerodynamic and aeroelastic problems about a wide range of geometries including wings, wing/fuselage, wing/control system, propulsion, and integrated airframe/propulsion configurations.[16–18]

ENS3DAE solves the full three-dimensional compressible Reynolds-averaged Navier–Stokes equations, the thin-layer approximation to these equations, or the Euler equations using an implicit approximate factorization algorithm. Central finite differences are used for spatial discretization, and a three-dimensional implementation of the Beam–Warming implicit scheme is employed for the temporal integration. Blended second- and fourth-order dissipation is added to the explicit right-hand side of the equations, and implicit second-order dissipation is added to improve the diagonal dominance of the matrix system. For time-accurate cases, global or local time stepping within an inner subiteration loop for each physical time step is employed. The subiteration procedure effectively removes the stability limit on the time step for unsteady flow cases and improves the temporal accuracy of the method, provided that relevant timescales within the computed flowfield are captured by the selected time step and that a sufficient number of subiterates are computed.

The method accepts either single- or multiple-block curvilinear grids. Boundary conditions are imposed explicitly on each computational face of each grid block, and the current release of the program requires a one-to-one match of grid points at block interfaces. Turbulence characteristics are predicted using the Baldwin–Lomax algebraic turbulence model or the Johnson–King model.[19] The code is written to take advantage of vectorization; directives for parallel operation on shared memory processors are also included in the programming. The method is regularly executed on eight or more processors.

A linear generalized mode shape structural model is closely coupled with the aerodynamic method to analyze structurally flexible vehicles. ENS3DAE uses a highly efficient, grid-motion algorithm for aeroelastic and control-surface simulations that is based on an algebraic shearing technique. Because dynamic aeroelastic and oscillating control surface simulations require grid models that deform in time, the algorithm now enforces the geometric conservation law.[20]

Results

The aeroelastic analysis is carried out with enforced consistency between velocity and dynamic pressure, assuming constant density and temperature at sea-level conditions ($\rho_\infty = 0.0023771$ slugs/ft^3 and $T_\infty = 518.67\,^\circ$R). Mach number and Reynolds number are treated as independent variables (unless otherwise specified), such that match-pointed conditions are not achieved. Assuming inviscid flow, match-pointed calculations are also carried out for different altitudes to document the attainability of LCO under realistic conditions. Reynolds number is not varied in this investigation and is specified to be 15×10^6. Structural damping and root angle of attack are assumed to vanish for all baseline cases investigated.

Summary of Grid Construction

Three grids are constructed for the CAPTSDv calculations reported in this paper. Owing to the geometry of the wing/store configuration and the midplane formulation of the surface boundary condition used in CAPTSDv, these grids are rectilinear. Clustering of grid points is enforced along the edges of the geometry and normal to the wing and store surfaces. Grids are generated by first computing grid-point distributions in each of the three coordinate directions external to CAPTSDv, subject to the specified clustering conditions, and then using the generator internal to CAPTSDv to obtain the full rectilinear grid. The first grid (G1) is used for inviscid, clean-wing, and wing/store (store mass only) computations; the second grid (G2) is used for inviscid, wing/store computations; and the third grid (G3) is used for viscous clean-wing and wing/store (store mass only) computations. The values of parameters governing grid construction are given in Table 1. A view of grid G2 in the x–y plane in the neighborhood of the wing/store configuration is shown in Fig. 2a to illustrate the effect of grid clustering along the combined planform.

For the ENS3DAE calculations presented in this paper, only the clean wing (to which the store mass can be added) is considered. A two-block, HH-type grid is used for this configuration and is generated with GRIDGEN V13. The two blocks have equal dimensions ($161 \times 71 \times 71$) and grid spacings and correspond to the
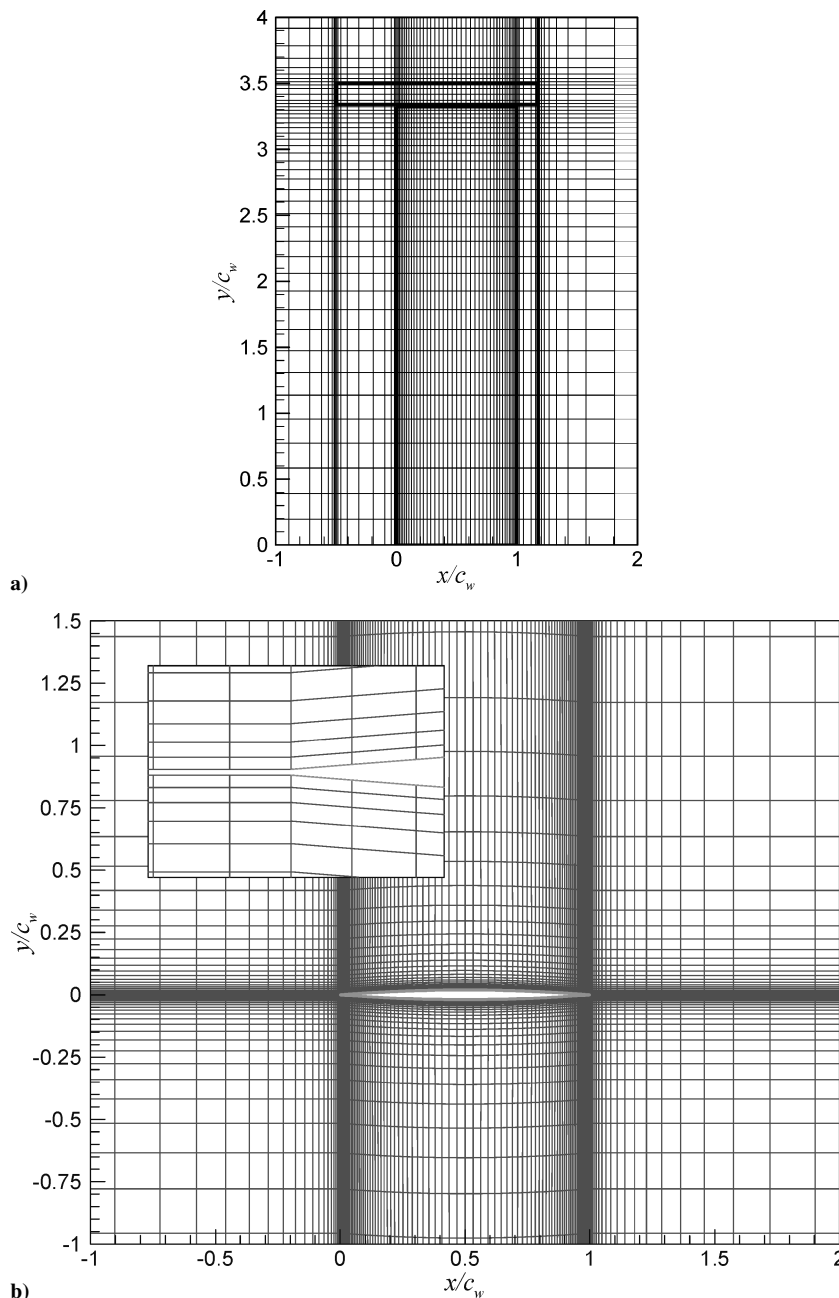

Fig. 2 CAPTSDv and ENS3DAE computational grids for Goland$^+$ wing: a) CAPTSDv wing surface grid (G2)—grid lines (red); wing boundary (green); store boundary (blue); b) ENS3DAE root-plane grid (inset figure shows leading edge)—grid lines (red); wing boundary (green).

Table 1 Selected values of CAPTSDv grid parameters (lengths in wing chords c_w)

Parameter	Grid G1	Grid G2	Grid G3
Domain size (x, y, z)	(41, 13.5, 40)	(41, 13.5, 40)	(41, 13.5, 40)
Grid dimensions (i, j, k)	(90, 55, 60)	(90, 55, 60)	(150, 55, 60)
Leading-edge spacing	0.01	0.01	0.008
Trailing-edge spacing	0.01	0.01	0.008
Normal spacing (top, bottom)	(0.002, 0.002)	(0.002,0.002)	(0.002,0.002)
Wing-tip spacing	0.025	0.025	0.025
Wing index dimensions (i, j)	(41, 32)	(41, 32)	(101, 32)
Store index dimensions (i, j)	N/A	(57, 5)	N/A

upper and lower halves of the computational space. The wing-tip geometry is slightly modified from the description just given to close the tip and simplify the grid-generation process. For inviscid calculations, the ENSDAE grid is somewhat finer than that used by CAPTSDv and places grid points about three times closer to the wing surface.

Figure 2b shows a portion of the grid in the root plane. The inset shows a highly magnified view of the leading edge and highlights a gap between the upper and lower blocks equal to 0.053% of the chord. A sharp leading edge is difficult to model using an Euler/Navier–Stokes solver; the gap helps by removing the leading edge from the computational domain. The leading edge is captured numerically through the boundary conditions applied at points around the physical leading edge. In the spanwise direction, the wing tip is modeled by transitioning the geometry from the full airfoil thickness at the wing tip to zero thickness at the first spanwise station outboard of the wing tip.

A systematic, grid-refinement study was not pursued for the dynamic aeroelastic results presented herein. However, previous grid-convergence studies by the authors and their colleagues established that static aerodynamic features were reasonably well converged in terms of the spacing of grid points. Furthermore, the time step selected for CAPTSDv dynamic analysis (0.1) was found to yield results that were reasonably well converged in time. [The same was true for ENS3DAE using a Courant–Friedrichs–Lewy (CFL) number of 50]. Grid sizes used in this study approximately followed those assumed in a previous code-evaluation investigation involving CAPTSDv, ENS3DAE, and another high-quality, national code, CFL3DAE.[19] In Ref. 19, several flight vehicles were carefully analyzed with these codes to simulate a number of aeroelastic phenomena. The selection of an HH-type grid topology was based on the mathematical formulation of CAPTSDv and the character of the wing cross section, which possesses sharp leading and trailing edges. The same topology was used in the ENS3DAE calculation to maintain consistency with the CAPTSDv analysis, to increase accuracy near the leading edge of the wing, and to build on ENS3DAE's past history with such grids.[17]

Modal Analysis

Modes of the structural model are computed with MSC/NASTRAN and then splined to aerodynamic surface grids (specified at $z = 0$) with the infinite plate spline, as implemented by Smith et al.[21,22] The modes are scaled to yield generalized masses of magnitude 1. Modal amplitudes are computed through time integration of the generalized structural dynamics equations to yield updated approximations of wing/store surface deflections. Unless otherwise stated, results given in this paper are obtained by retaining the four modes of lowest frequency in the aeroelastic analysis and by excluding in-plane modes. Sets of retained of modes are shown in Fig. 3 for two cases: clean wing with no store and wing with store mass positioned 1.75 ft forward of the wing elastic axis (see following discussion). With the exception of mode 4, the modes in the two sets are quite similar; slightly more torsion is evident at the wing tip in the modes associated with the clean wing.

Linear Analysis

To determine a parameter space (velocity and Mach number for specified altitude) where store-induced LCO possibly exists, a linear flutter analysis of a clear wing and a wing/tip store combination is conducted. The linear flutter speeds (those from linear aerodynamic theories) are determined from data calculated from the p-k method of MSC/NASTRAN. The flutter and divergence instabilities can be determined from an inspection of calculated data in graphical form, the so-called V-g and V-ω diagrams. These diagrams are shown in Fig. 4 for the clean wing and the wing with tip store mass for Mach 0.92. From Fig. 4a, the flutter speed of the clean wing (334 ft/s) is determined by the first crossing of one of the modes (mode 1) from negative to positive values of the damping parameter g and a corresponding flutter frequency of 2.17 Hz. Additionally, shown in Figs. 4a is a divergence instability, whose speed (630 ft/s) is determined by the simultaneous occurrence of zero damping and zero frequency for another mode (mode 2). The two eigenvalues corresponding to mode 2 become real at a flight speed of about 520 ft/s (see Fig. 4c) and move apart from one another at higher speeds, with one eigenvalue ultimately causing divergence, as just described.

The V-g and V-ω diagrams of the wing with tip store mass are shown in Figs. 4b and 4d, respectively, when the store c.g. is located 1.75 ft upstream of the wing ea (equivalent to the store pitch axis). In Fig. 4b, it is seen that the flutter speed is increased to 559 ft/s when the store c.g. is placed at this position and that the severity of the flutter instability of the clean wing has been reduced (reflected by less damping). The flutter mode of the wing/store has been converted into a hump, or lightly damped mode. Following Denegri,[1] it is speculated that the initiation of store-induced LCO is associated, in some way, with hump modes, such that the linear flutter investigation defined a beginning region to search for LCO. Of course, the region of LCO must be modified to account for transonic nonlinearities because this hump is determined from linear aerodynamics. This modification is discussed in the following sections for a determination of store-induced LCO.

Linear analysis is carried out for other store mass positions, but not reported herein. These results show the reduction of the peak damping parameter with forward movement of the store mass. The offset position of 1.75 ft (upstream of the wing ea) is selected for use in the CAPTSDv calculations reported next because of the small peak value of g attained with this parameter value.

Flutter Boundaries

Boundaries of flutter and LCO onset are computed for the clean-wing configuration and for the wing with tip store mass (i.e., store not modeled aerodynamically). The flow is assumed to be inviscid. These results are compared to those obtained with MSC/NASTRAN using linear analysis. LCO solutions are observed at Mach numbers above Mach 0.9 when the store mass is present; these cases will be discussed in greater detail in the next section. Flutter and LCO boundaries are compared in Fig. 5a. For the clean wing, CAPTSDv predicts a flutter speed of 433 ft/s at Mach 0.7, a value 3.5% higher than that predicted by MSC/NASTRAN. With the store mass included, CAPTSDv predicts a flutter speed of 648.5 ft/s (CAPTSDv), a value 6.8% higher than that provided by MSC/NASTRAN. At Mach 0.7, the aerodynamics are linear, and the reasonable comparisons between CAPTSDv and MSC/NASTRAN are to be expected. CAPTSDv clearly confirms that forward movement of the store mass has a stabilizing effect on the aeroelastic system for Mach numbers at or below 0.9.

As Mach number increases beyond 0.7, the clean-wing flutter boundary obtained with CAPTSDv develops a transonic dip with a minimum flutter speed (355 ft/s) at about Mach 0.88. The boundary is much flatter when the store mass is included; flutter speed averages around 645 ft/s. Both boundaries show a rapid increase in flutter speed near Mach 0.9. However, at selected Mach numbers between 0.90 and 0.95 (0.91, 0.92, 0.93, and 0.94) with the store mass present LCO solutions are observed. These nonlinear oscillations are computed at flight speeds much lower than the nominal, wing/store flutter speed, and, for some Mach numbers, lower than

Mode 1
1.97 Hz

Mode 2
4.05 Hz

Mode 3
9.65 Hz

Mode 4
13.4 Hz

a)

Mode 1
1.69 Hz

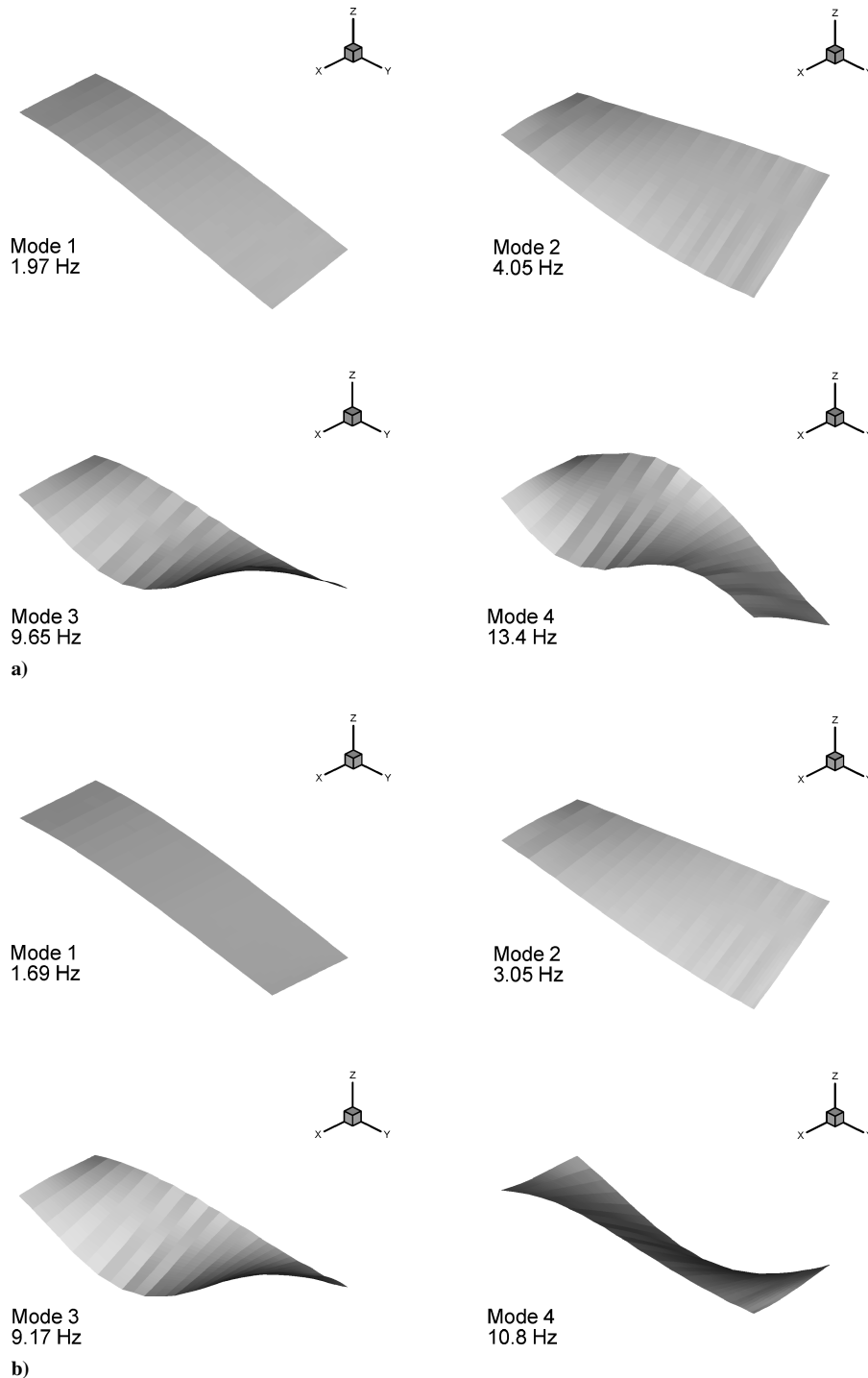Mode 2
3.05 Hz

Mode 3
9.17 Hz

Mode 4
10.8 Hz

b)

Fig. 3   Splined modes retained in aeroelastic analysis of Goland⁺ wing with and without store mass: a) clean wing and b) wing with store mass (offset 1.75 ft forward).

the clean-wing flutter speed. Thus, the presence of the store destabilizes the system at higher Mach numbers in an adverse manner, that is, to lower flight speeds.

On the flutter boundary for the wing/store configuration, two different flutter modes are observed. These are contrasted in terms of the computed lift and moment coefficients (taken about the leading edge) for Mach 0.84 and Mach 0.9, as shown in Figs. 5b and 5c. Note that unstable test points are selected above the flutter boundary: $U = 750$ ft/s at Mach 0.84 (flutter at 642.5 ft/s) and $U = 850$ ft/s at Mach 0.9 (flutter at about 825 ft/s). Two different frequencies of divergent oscillation are observed: 1.90 Hz (Mach 0.84) and 9.52 Hz (Mach 0.90). These frequencies are somewhat larger than the natural frequencies corresponding to modes 1 (1.69 Hz) and 3 (9.17 Hz),

respectively. For both flutter modes, the phase relationships between peak lift and moment are the same (about 180 deg out of phase). Differences in frequency correlate well with differences in modal participation between the flutter modes. As shown in Figs. 5d and 5e, response is dominated by modes 1 and 2 at Mach 0.84, whereas modes 3 and 4 dominate the response at Mach 0.9. The impact of varying modal participation on wing shape is described in the next section.

A switching of flutter modes is perhaps suggested by the linear MSC/NASTRAN results shown for Mach 0.92 in Fig. 4. (The results for Mach 0.9 are not markedly different.) The effect of nonlinearity appears to be large in terms of stabilizing the interaction between modes 1 and 2, predicted by MSC/NASTRAN to occur at about
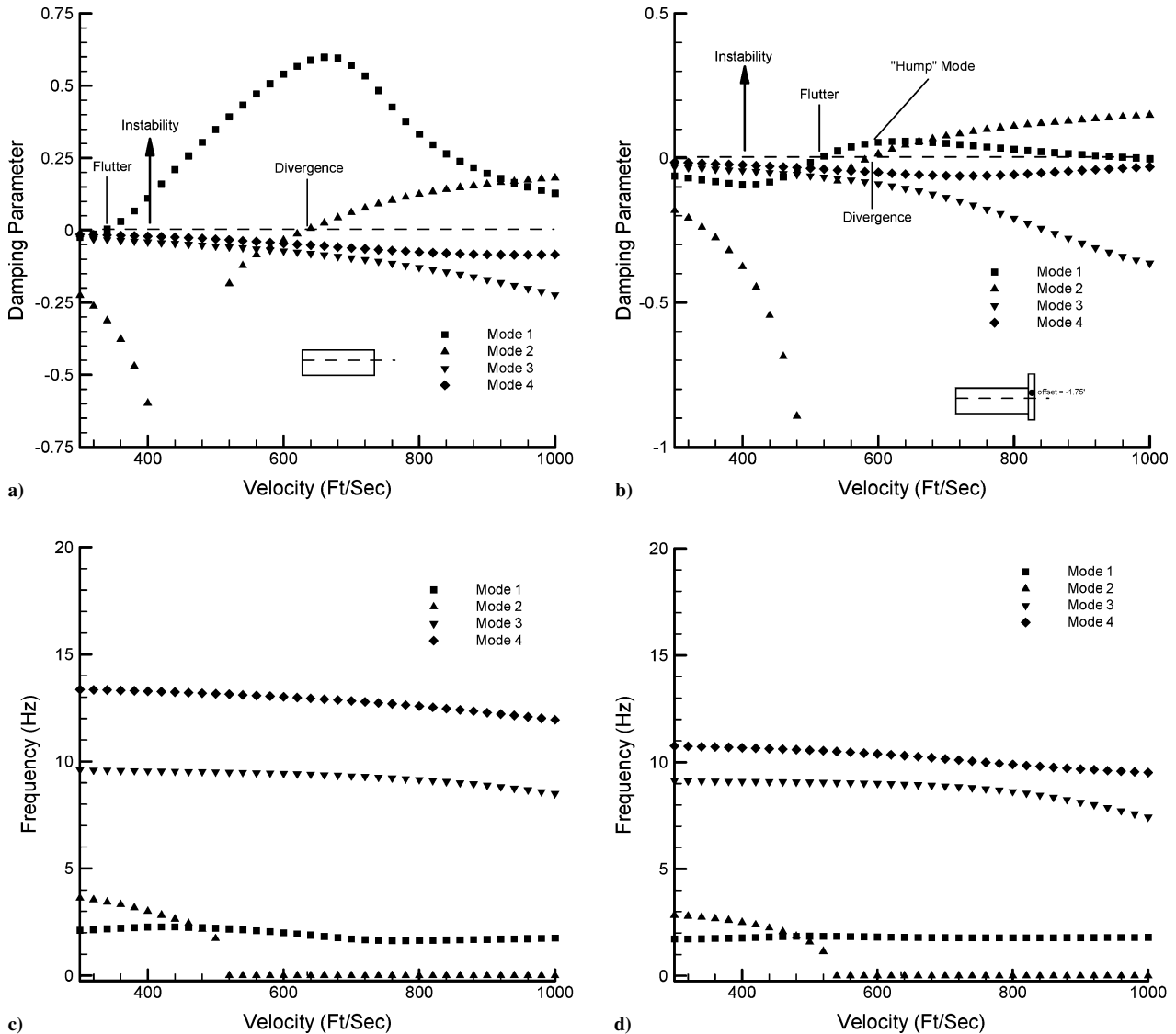
Fig. 4   Damping and frequency characteristics predicted by linear aeroelastic analysis (MSC/NASTRAN) for the Goland⁺ wing with and without store mass at Mach 0.92: a) clean-wing damping; b) wing/store damping; c) clean-wing frequencies; and d) wing/store frequencies.

560 ft/s. At a larger frequency, coalescence of modes 3 and 4 is evident in the MSC/NASTRAN results at a flight speed of about 800 ft/s, a velocity near the flutter speed predicted by CAPTSDv.

Store-Induced Limit-Cycle Oscillation

In a Mach-number range between 0.91 and 0.95, fully developed LCO states are computed with CAPTSDv for the wing/store configuration, excluding store aerodynamics (see Fig. 5a). As will be shown later, the effect of including store aerodynamics is not significant, while the effect of viscosity is to reduce LCO amplitude. Two types of LCO are observed: 1) an expected form involving significant time-periodic oscillations of the aeroelastic system that will be described first and referred to as simply LCO, and 2) an unexpected form with very small amplitudes (approximately three orders of magnitude less in magnitude) that will be described second and referred to as "embryonic" LCO, or ELCO.

As shown in Fig. 5a, LCO is observed over a restricted range of Mach numbers. Generally, LCO amplitudes increase with increasing velocity, and for sufficiently large velocities computed oscillations become so large that the assumptions of TSDT become invalid. Attention is first given to Mach 0.92, where LCO is first observed at $U = 390$ ft/s for inviscid flow (onset occurring between 385 and 390 ft/s) and $U = 410$ ft/s for viscous flow (onset occurring between 390 and 410 ft/s). The onset of LCO is computationally expensive

to obtain because very large integration times are necessary for the aeroelastic system to approach time-asymptotic behavior at values of flight speed near critical. In these calculations, the initial state is defined by a flow solution given by a rigid-body calculation, and the modal amplitudes are assumed to vanish, except for the first mode, which is assigned an initial value of 0.01.

LCO grows slowly in time, becoming fully developed with a frequency of 2.92 Hz at about 40 time units for $U = 410$ ft/s and Mach 0.92 assuming inviscid flow. Time histories of fully developed lift and moment coefficient are shown in Fig. 6a. The phase relationship between these quantities is similar to that observed for the two flutter modes described earlier. The computed frequency corresponds to the modal content of the aeroelastic response. As seen in Fig. 6b, mode 2 (a natural frequency of 3.05 Hz) dominates the response, with strong participation also from mode 1. At this Mach number and flight speed, the first two modes are much more strongly coupled than in the flutter mode found at low transonic Mach numbers (compare Mach 0.84), with an associated increase in response frequency.

LCO develops in a similar manner for the case of viscous flow, as shown in Fig. 7 for an equivalent flight speed of 410 ft/s and Mach 0.92. Grid G3 is used for viscous calculations, and the aerodynamics of the store are assumed negligible. LCO amplitude is observed to diminish through the effects of viscosity, and frequency slightly increases to 2.99 Hz. Viscous simulations of LCO are somewhat
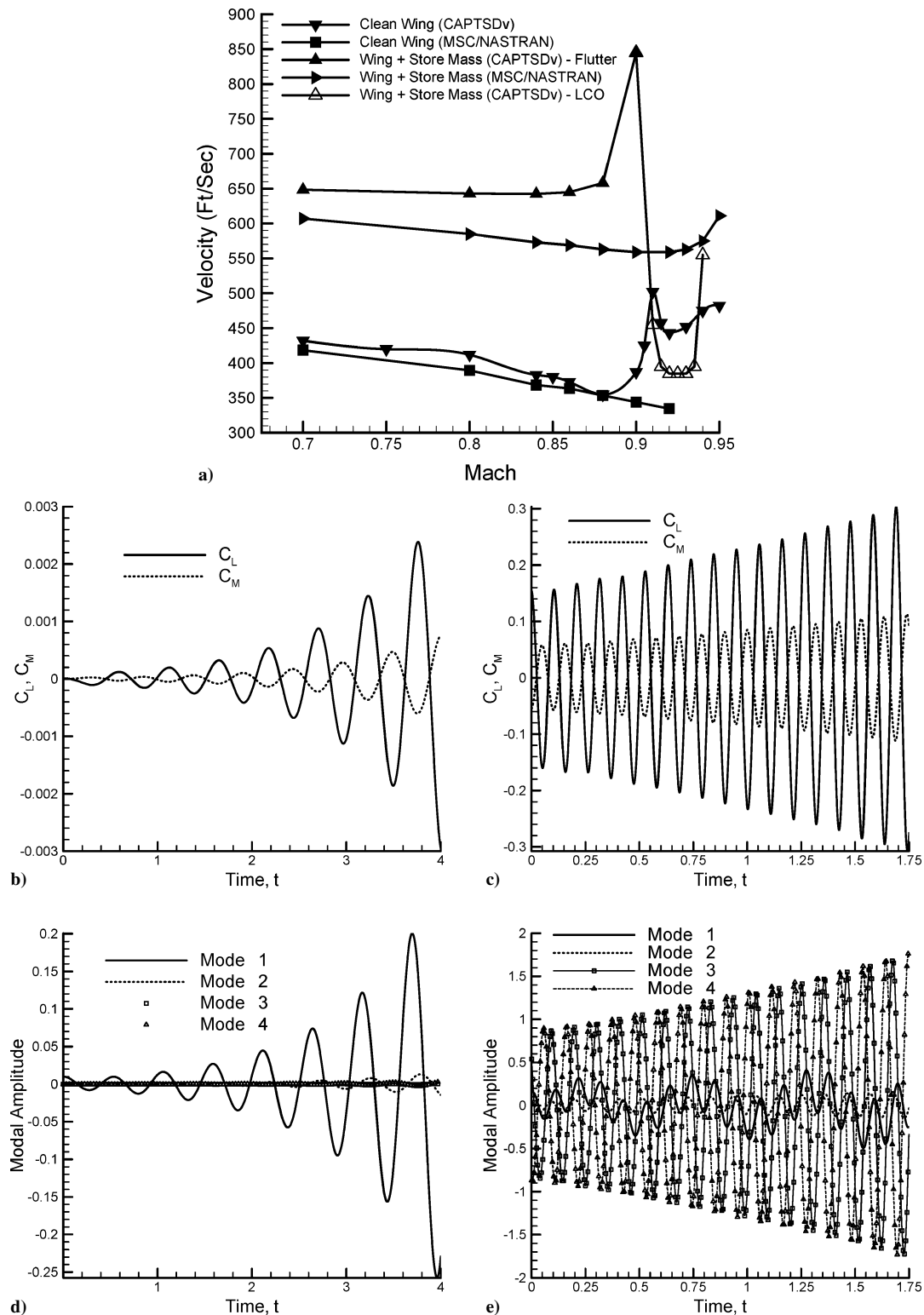
Fig. 5   Inviscid CAPTSDv aeroelastic analysis for grid G1 without store aerodynamics: a) comparison of flutter and LCO boundaries computed with CAPTSDv and MSC/NASTRAN; b) and c) force and moment coefficient histories for Mach 0.84 ($U = 750$ ft/s) and Mach 0.90 ($U = 850$ ft/s); d) and e) modal amplitude histories for Mach 0.84 ($U = 750$ ft/s) and Mach 0.90 ($U = 850$ ft/s).

stiffer than inviscid computations, requiring one Newton subiterate per time step for stable calculation.

Structural response associated with LCO is contrasted with that of the two flutter modes through visualization of wing-tip motion. Snapshots of instantaneous chordline orientation (lines connecting wing tip leading edge and trailing edge) are shown in Fig. 8 for each of the three characteristic aeroelastic responses computed with CAPTSDv (inviscid) and described earlier. The low-speed flutter mode is primarily first bending, which is reflected by a vertical

displacement of the wing tip at different times, with introduction of only a slight incidence angle with respect to the freestream. The flutter mode observed at Mach 0.9 is a higher-frequency mode involving significant contributions from modes 3 and 4. The response of the wing tip involves both pitch and plunge and a visual rotation approximately about the midchord. In the situation of LCO at Mach 0.92, the response is composed of first bending and first torsion contributions. A pitching motion dominates the resulting movement of the wing tip, with visual rotation about the tip leading edge.
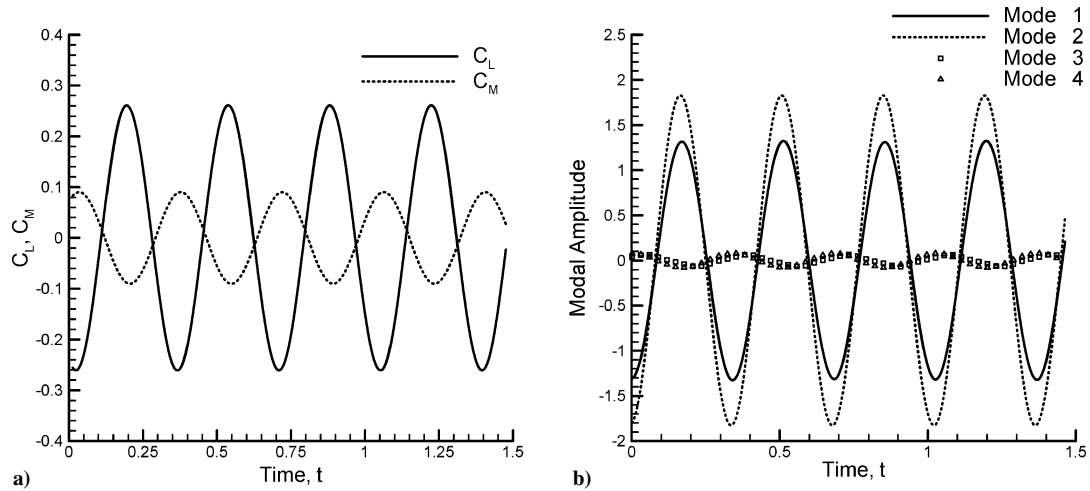
Fig. 6   Inviscid CAPTSDv aeroelastic analysis for grid G1 without store aerodynamics at Mach 0.92 and $U = 410$ ft/s: a) temporal variations of lift and moment coefficients during LCO and b) modal amplitudes during LCO.
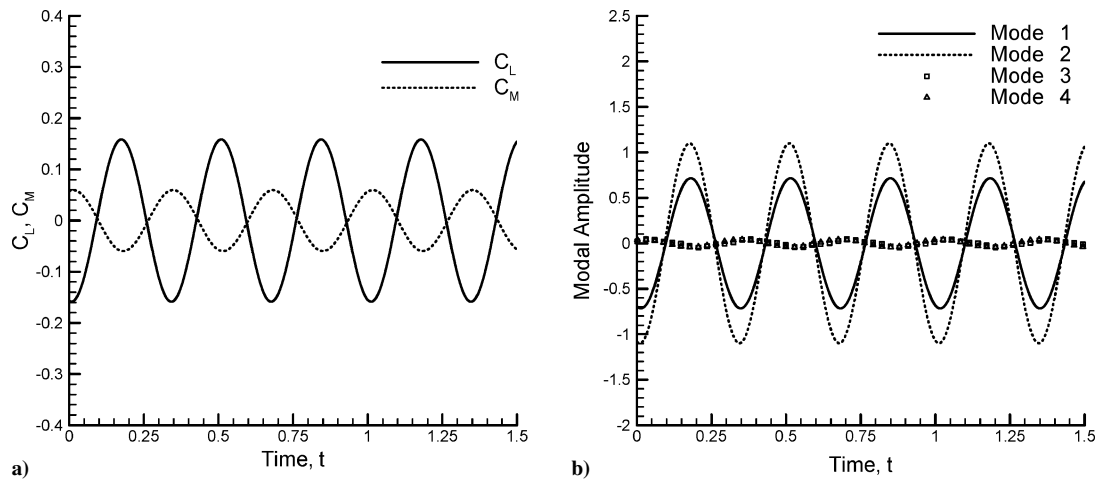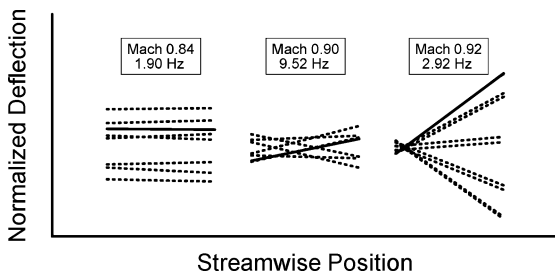

Fig. 7   Viscous CAPTSDv aeroelastic analysis for grid G3 without store aerodynamics at Mach 0.92 and $U = 410$ ft/s: a) temporal variations of lift and moment coefficients during LCO and b) modal amplitudes during LCO.

Fig. 8   Snapshots of wing-tip chordlines (grid G1) for three characteristic aeroelastic responses computed with CAPTSDv (inviscid): flutter at Mach 0.84 ($U = 750$ ft/s); flutter at Mach 0.90 ($U = 850$ ft/s); and LCO at Mach 0.92 ($U = 410$ ft/s). The maximum deflections for the three responses shown are 0.025, 0.15, and 0.5 ft, respectively.

LCO solutions of the type just described are not observed at flight speeds below 390 ft/s for inviscid flow at Mach 0.92. However, at speeds between 340 and 390 ft/s sustained oscillations of very small amplitude and less regular character are computed. In this speed range, the magnitude of system oscillations increases very slowly with increasing U. These ELCO states appear to be physical and not numerical in origin because ELCO formation persists while Mach number and various numerical parameters are varied. However, ELCO amplitude is sensitive to structural damping and the numerical precision of the computation. When ζ is increased from

the baseline value of 0 to 0.03, ELCO amplitude is reduced by over a factor of 5 at $U = 385$ ft/s and is found to vanish at $U = 350$ ft/s. Also, when the precision of the computation is increased to double (single precision is baseline) ELCO amplitude is observed to grow considerably, but remains small compared to LCO amplitude. A time history of lift coefficient is shown in Fig. 9 for $U = 385$ ft/s and assuming baseline values of numerical parameters: the frequency of 2.94 Hz is nearly identical to that found during LCO at $U = 410$ ft/s, while peak lift coefficient reaches only about 5×10^{-5}.

Owing to their small magnitude, these ELCOs bear resemblance to the shock-induced oscillations described by Edwards.[13] The time-dependent distributions of surface pressure for ELCO cases should be further analyzed to determine if upstream propagating Mach waves strongly participate in this aeroelastic response.

LCO Sensitivities

The variation of LCO amplitude with respect to changes in flight speed at Mach 0.92 is computed for three categories of analysis: inviscid analysis of wing with store mass (grid G1), inviscid analysis of wing with store modeled aerodynamically (grid G2), and viscous analysis of wing with store mass (grid G3). Results are compared in Fig. 10 to show the effects of varying the level of modeling fidelity within the context of transonic small-disturbance theory. Assuming inviscid flow, it is observed that modeling the store aerodynamically has little impact on the onset or computed amplitude of LCO. However, at speeds exceeding 420 ft/s solutions cannot be stably
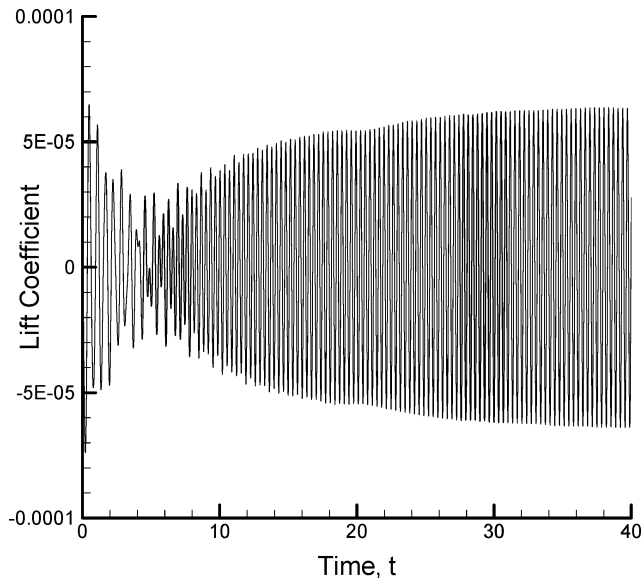
Fig. 9 Low-amplitude oscillations at Mach 0.92 and $U = 385$ ft/s (grid G1).

Fig. 11 Comparison of LCO response boundaries for selected angles of attack assuming inviscid analysis without store aerodynamics at Mach 0.93.
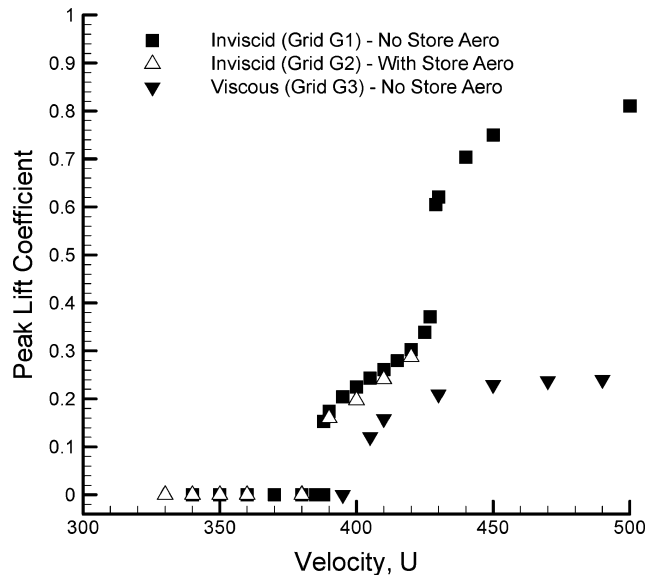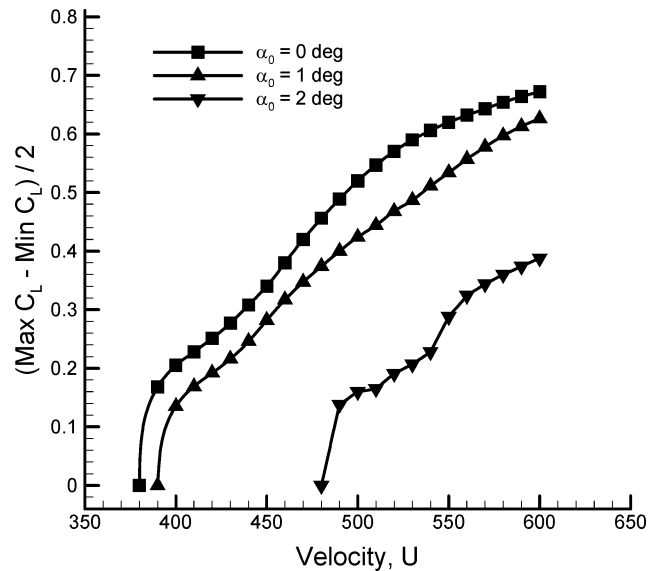

Fig. 10 Comparison of LCO response boundaries at Mach 0.92 for inviscid analysis without inclusion of store aerodynamics (grid G1), with store aerodynamics (grid G2), and viscous analysis without store aerodynamics (grid G3).

computed. In these cases of increased wing-tip twist, numerical destabilization appears to be a result of a very large, localized, pressure spike observed in the region of the juncture between the store and the wing leading edge. This destabilization occurs at about the speed for which LCO amplitude is predicted to grow rapidly when store aerodynamics are ignored; peak lift coefficient begins to take a large jump at $U = 427$ ft/s with this approximation. At speeds exceeding this value, the validity of the computed inviscid solutions appears diminished, owing to the small-disturbance nature of the methodology. As just described above for $U = 410$ ft/s, the effect of viscosity is to diminish LCO amplitude. When the boundary-layer thickness is modeled, no large increase in LCO amplitude is observed, and peak lift coefficient remains bounded by 0.26 over the range of speeds examined, thus reducing the deformation of the wing and extending the speed range over which the assumption of small disturbances is arguably satisfied. The phenomenon of saturation in the growth of LCO amplitude was investigated more thoroughly by Beran et al.[23] and found to be a result of shock-boundary-layer

interaction. In their study, trailing-edge separation of the boundary layer retarded the movement of shocks on the upper and lower surfaces of the wing that would be quite substantial if viscosity were neglected. When the range of shock motions was confined, the pressure differentials needed to support large-amplitude LCOs could not be sustained.

Near the bifurcation point, at $U = 388$ ft/s, nonunique states are observed for inviscid analysis of the wing with store mass (grid G1). One state, obtained with the baseline initial conditions, exhibits very small-amplitude ELCO behavior, whereas the other state, obtained by restarting the aeroelastic solution from $U = 390$ ft/s, exhibits LCO behavior. However, as velocity is reduced below 388 ft/s only ELCO is observed, and as velocity is increased above this same speed only LCO is observed. These results are indicative of the presence of a subcritical bifurcation just above this speed, causing relatively large jumps in LCO amplitude over a small range of flight speeds. This phenomenon is explored further next for Mach 0.93.

The variation of peak lift coefficient with velocity is found to be more regular at Mach 0.93 than at Mach 0.92. For this higher Mach number, the effects of variation of root angle of attack are assessed in Fig. 11 using the observed half-differentials between maximum and minimum lift coefficient (to separate the dependence of oscillation amplitude on velocity from the dependence of static aeroelastic response on velocity). When α_0 is increased to 2 deg, a considerable decrease in LCO amplitude is observed at specified velocities by significantly delaying LCO onset to higher velocities. However, if the shift to higher velocities is accounted for, the reduction in LCO amplitude decreases (to about 25% for $\alpha_0 = 2$ deg). Tang and Dowell[24] have also investigated the effects of angle of attack on LCO development. In their delta-wing plate model, nonlinearity in the structure is considered, while the aerodynamics are modeled linearly. It is interesting to note their finding that increasing pitch angle tends to diminish LCO amplitude at a fixed speed above critical. The reduction appears to be much larger than what was observed in this study, suggesting that the dynamic nonlinearities have greater relative strength than that of the aerodynamics for this limited comparison of results over different configurations.

As just stated for the results computed at Mach 0.92 (compare Fig. 10) assuming inviscid flow, the onset of LCO is subcritical. This is also observed at Mach 0.93, as shown in detail in Fig. 12 (for the baseline condition of vanishing root angle of attack). For this comparison, aeroelastic solutions are computed using two kinds of initial conditions: the initial conditions just described and initialization of the flowfield using a fully developed LCO solution obtained at a higher velocity. It is seen that the latter class of initial condition
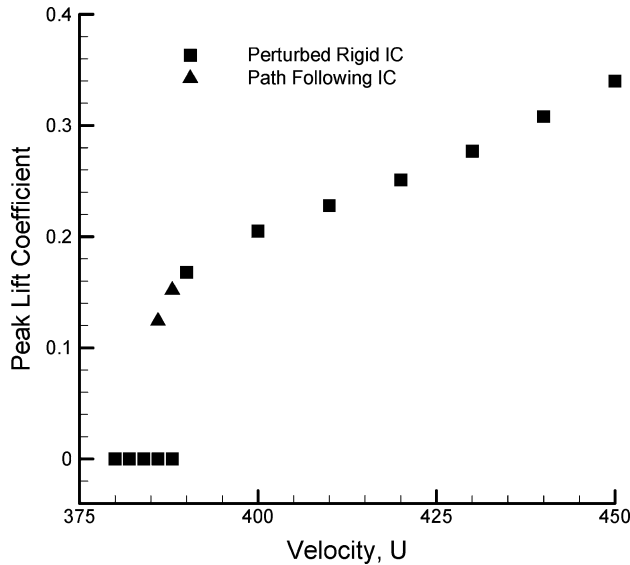
Fig. 12 Demonstration of subcritical Hopf bifurcation and nonunique aeroelastic behavior at Mach 0.93 (wing/store model without store aerodynamics). Two initial conditions are employed: baseline initial conditions (perturbed rigid IC) and converged LCO solutions at higher velocities (path following IC).

Fig. 14 LCO amplitudes as functions of altitude and Mach number for selected Mach numbers using matched-point analysis.
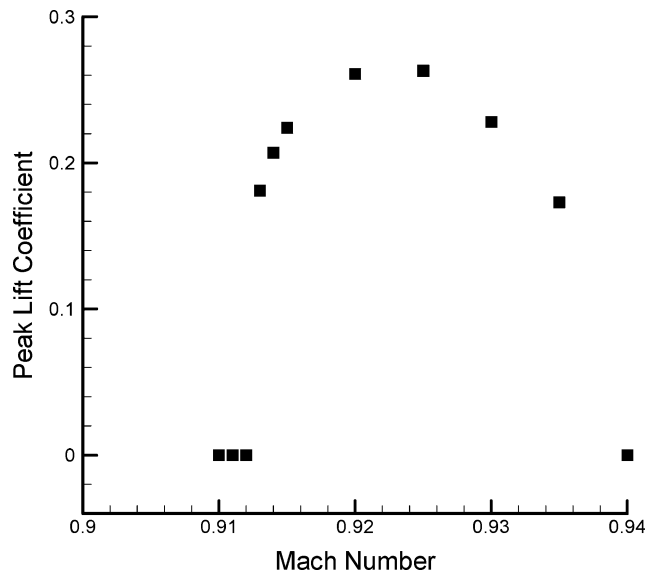

Fig. 13 Variation of LCO response for different Mach numbers at $U = 410$ ft/s (wing/store model without store aerodynamics).

produces fully developed LCO solutions for a small range of velocities (noted at 386 and 388 ft/s) at which the former class of initial condition does not produce LCO. Although the range of hysteresis is slight, the subcritical nature of the bifurcation does explain the rather large jumps in amplitude observed beyond the critical points.

Not surprisingly, over the range of Mach numbers that sustain LCO, amplitude of response is found to be highest over the midsection of the range. This is shown in Fig. 13 for a velocity of 410 ft/s. The response near the low-Mach boundary of the LCO region is characteristic of the subcritical response shown in Figs. 10 and 12. However, at the high-Mach boundary of the LCO region the computed results are not suggestive of nonunique flow responses.

Matched-Point Analysis

In the preceding analysis, flight speeds and Mach numbers are independently varied while assuming a constant density (sea-level conditions), resulting in inconsistent selections of parameter values. To determine if LCO solutions are physically realizable in flight
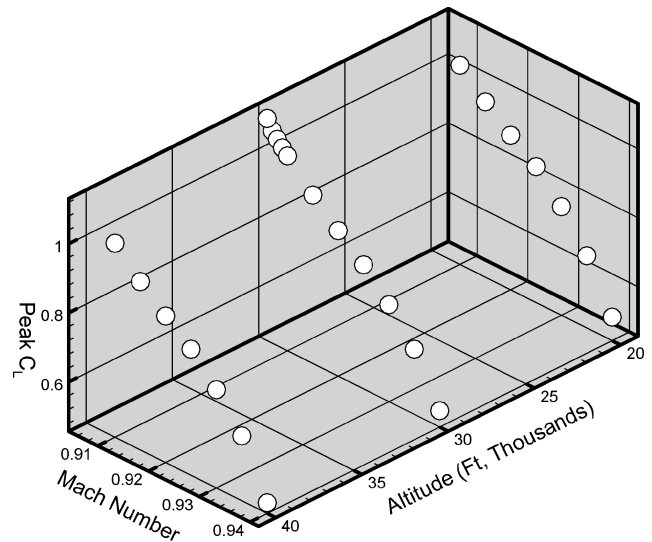
conditions for the Goland$^+$ wing with tip store mass, a matched analysis is pursued in which Mach number is consistently varied with flight speed for selected altitudes. Results are summarized in Fig. 14, where it is seen that the existence of LCO, expressed in terms of peak lift coefficient, is reasonably bounded over a certain altitude-Mach range: at and above 20,000 ft and between about Mach 0.905 and Mach 0.93. In this figure, only LCO states for which amplitudes do not become too large, about 1.0 or less, are shown. It is suspected that at or above the largest peak values of lift coefficient the aeroelastic responses would normally be thought of as flutter owing to the large angular deflections of the wing tip (approximately 15 deg or more). The onset of flutter (divergence or sustained, lift-coefficient oscillations larger than about 1.0), which would occur at Mach numbers lower than that represented by the data in Fig. 14, was not systematically evaluated and the corresponding data not shown. At values of Mach number larger than that presented in Fig. 14, aeroelastic oscillations died out, indicating stability of the wing/store configuration.

Of potential significance is the situation that LCO states diminish in amplitude as flight speed increases, such that flutter would be encountered first during test. The linear flutter speeds and Mach numbers predicted by MSC/NASTRAN, assuming matched analysis, are conservative: Mach 0.751 (10,000 ft), Mach 0.798 (20,000 ft), and Mach 0.892 (30,000 ft). In contrast to the results presented herein, Khot et al.[25] have investigated other streamwise positions of the tip store mass with matched analysis and observed (e.g., with the mass offset 1 ft upstream of the wing ea) that LCO responses of relatively small amplitude can occur at flight speeds below those normally corresponding to flutter.

Comparisons with ENS3DAE

To assist in the validation of the transonic aeroelastic modeling employed in CAPTSDv, CAPTSDv solutions (inviscid) are compared to ENS3DAE (Euler) solutions for two clean-wing calculations: prediction of static aeroelastic response for a root angle of attack of 2 deg and dynamic response of a rigid wing undergoing 3-Hz pitch oscillations of $\frac{1}{2}$ deg in amplitude. Both cases show good agreement between the Euler and TSDT results and are reported here for a transonic condition ($U = 400$ ft/s and Mach 0.92) in terms of the predicted values of lift and moment coefficients. For the case of static aeroelastic response, C_L predictions agree within 6% (0.126 for ENS3DAE and 0.134 for CAPTSDv) and C_M predictions agree within 15% (−0.0687 for ENS3DAE and −0.0809 for CAPTSDv). In the case of response to forced pitch oscillations, predictions of peak C_L agree within 3% (0.0411 for ENS3DAE and 0.0423 for CAPTSDv) and predictions of peak C_M agree within 4% (0.0153 for ENS3DAE and 0.0148 for CAPTSDv). Predicted

phase relationships between the lift and moment coefficients are also observed to be in close agreement.

Time-dependent solutions exhibiting LCO have also been computed using Euler fluid dynamics (ENS3DAE) for the Goland[+] wing with store mass but without store aerodynamics for Mach numbers and flight speeds similar to that studied with CAPTSD.[26] LCOs involving coupling between modes 1 and 2 are also predicted with ENS3DAE and compared in detail to CAPTSDv solutions.[26]

Summary

A class of limit-cycle oscillations (LCOS) was observed for a rectangular wing with tip store. These LCOs occurred at speeds lower than that predicted using linear aerodynamics and at speeds lower than that computed for the clean-wing configuration. The form of the bifurcation was subcritical, such that LCO amplitude jumped abruptly as Mach number increased beyond a critical value. However, as Mach number increased to a critical value (approximately 0.94–0.95), LCO states could no longer be sustained. For the configurations examined, the presence of LCO was insensitive to the inclusion of store aerodynamics in the aeroelastic model. Also, the effect of viscosity was to diminish LCO amplitude. A second class of LCO solutions with small amplitude was observed that occurred over a range of speeds below critical, that is, prior to the initiation of LCOs characterized by large-amplitude aeroelastic response. These states were found to be sensitive to structural damping, such that addition of nominal levels of damping was sufficient to overcome the phenomenon.

The search for LCO states was conducted in two steps. First, linear theory was employed in the identification of hump modes, which corresponded to placement of the store mass near the wing leading edge. Such characteristic aeroelastic responses were expected to point to conditions susceptible to LCO. Second, LCO states were computed using the transonic small-disturbance theory algorithm CAPTSDv, assuming both inviscid and viscous flow. This nonlinear mathematical formulation was sufficient to capture properly weak shock formation and movement.

The qualitative nature of the LCO results reported herein has been validated using a higher-fidelity method based on the Euler equations.[26] Promising agreement between LCO onset speed, frequency, and modal content was observed. Static aeroelastic and dynamic rigid responses of the clean wing computed with CAPTSDv and ENS3DAE were compared in this paper and found to be in good agreement.

Future work is planned for the validation of LCOs computed with CAPTSDv assuming viscous flow. Also, further investigation is required to yield a full explanation of LCO development for the wing/store configuration examined herein and to better understand any potential connection between the observed nonlinear LCO phenomenon and the development of hump modes in the reported linear analysis.

Acknowledgments

References

[1]Denegri, C. M., "Limit Cycle Oscillation Flight Test Results of a Fighter with External Stores," *Journal of Aircraft*, Vol. 37, No. 5, 2000, pp. 761–769.

[2]Turner, C. D., "Effect of Store Aerodynamics on Wing/Store Flutter," *Journal of Aircraft*, Vol. 19, No. 7, 1982, pp. 574–580.

[3]Gern, F. H., and Librescu, L., "Static and Dynamic Aeroelasticity of Advanced Aircraft Wings Carrying External Stores," *AIAA Journal*, Vol. 36, No. 7, 1998, pp. 1121–1129.

[4]Eastep, F. E., and Olsen, J. J., "Transonic Flutter Analysis of a Rectangular Wing with Conventional Airfoil Sections," *AIAA Journal*, Vol. 17, No. 10, 1980, pp. 1159–1164.

[5]Melville, R., "Nonlinear Simulation of F-16 Aeroelastic Instability," AIAA Paper 2001-0570, Jan. 2001.

[6]Melville, R., "Nonlinear Mechanisms of Aeroelastic Instability for the F-16," AIAA Paper 2002-0871, Jan. 2002.

[7]Farhat, C., Pierson, K., and Degand, C., "CFD Based Simulation of the Unsteady Aeroelastic Response of a Maneuvering Vehicle," AIAA Paper 2000-0899, Jan. 2000.

[8]Batina, J. T., "Efficient Algorithm for Solution of the Unsteady Transonic Small-Disturbance Equation," *Journal of Aircraft*, Vol. 25, No. 7, 1988, pp. 598–605.

[9]Batina, J. T., "Unsteady Transonic Algorithm Improvements for Realistic Aircraft Applications," *Journal of Aircraft*, Vol. 26, No. 2, 1989, pp. 131–139.

[10]Batina, J. T., "A Finite Difference Approximate-Factorization Algorithm for Solution of the Unsteady Transonic Small-Disturbance Equation," NASA TP 3129, Jan. 1992.

[11]Howlett, J. T., "Efficient Self-Consistent Viscous Inviscid Solution for Unsteady Transonic Flow," *Journal of Aircraft*, Vol. 24, No. 11, 1987, pp. 737–744.

[12]Edwards, J. W., "Transonic Shock Oscillations Calculated with a New Interactive Boundary Layer Coupling Method," AIAA Paper 93-0777, Jan. 1993.

[13]Edwards, J. W., "Calculated Viscous and Scale Effects on Transonic Aeroelasticity," *Numerical Unsteady Aerodynamic and Aeroelastic Simulation*, North Atlantic Treaty Organization, AGARD-R-822, March 1998, pp. 1-1–1-11.

[14]Green, J. E., Weeks, D. J., and Brooman, J. W. F., "Prediction of Turbulent Boundary Layers and Wakes in Compressible Flow by a Lag-Entrainment Method," British Aeronautical Research Council, R&M No. 3791, London, 1977.

[15]Schuster, D. M., Vadyak, J., and Atta, E., "Static Aeroelastic Analysis of Fighter Aircraft Using a Three-Dimensional Navier–Stokes Algorithm," *Journal of Aircraft*, Vol. 27, No. 9, 1990, pp. 820–825.

[16]Smith, M. J., Schuster, D. M., Huttsell, L. J., and Buxton, B., "Development of and Euler/Navier–Stokes Aeroelastic Method for Three-Dimensional Vehicles with Multiple Flexible Surfaces," AIAA Paper 96-1400, April 1996.

[17]Schuster, D. M., Beran, P. S., and Huttsell, L. J., "Application of the ENS3DAE Euler/Navier–Stokes Aeroelastic Method," *Numerical Unsteady Aerodynamic and Aeroelastic Simulation*, North American Treaty Organization, AGARD-R-822, March 1998, pp. 3-1–3-11.

[18]Lewis, A. P., and Smith, M. J., "Euler-Based Aeroelastic Analysis of Shell Structures," *Journal of Aircraft*, Vol. 37, No. 5, 2000, pp. 840–845.

[19]Huttsell, L., Schuster, D., Volk, J., Giesing, J., and Love, M., "Evaluation of Computational Aeroelasticity Codes for Loads and Flutter," AIAA Paper 2001-0569, Jan. 2001.

[20]Thomas, P. D., and Lombard, C. K., "Geometric Conservation Law and Its Application to Flow Computations on Moving Grids," *AIAA Journal*, Vol. 17, No. 10, 1979, pp. 1030–1037.

[21]Smith, M. J., Hodges, D. H., and Cesnik, C. E. S., "An Evaluation of Computational Algorithms to Interface Between CFD and CSD Methodologies," WL-TR-96-3055, Wright–Patterson Air Force Base, Nov. 1995.

[22]Smith, M. J., Hodges, D. H., and Cesnik, C. E. S., "Evaluation of Computational Algorithms Suitable for Fluid-Structure Interactions," *Journal of Aircraft*, Vol. 37, No. 2, 2000, pp. 292–294.

[23]Beran, P. S., Khot, N. S., Eastep, F. E., Strganac, T. W., and Zweber, J. V., "Effects of Viscosity on Store-Induced Limit-Cycle Oscillation," *Proceedings of the 2003 ITEA Aircraft-Stores Compatibility Symposium XIII*, International Test and Evaluation Association, Fairfax, VA, Feb. 2003.

[24]Tang, D., and Dowell, E. H., "Effects of Angle of Attack on Nonlinear Flutter of a Delta Wing," *AIAA Journal*, Vol. 39, No. 1, 2001, pp. 15–21.

[25]Khot, N. S., Beran, P. S., Zweber, J. V., and Eastep, F. E., "Influence of Tip Store Mass Location on Wing Limit-Cycle Oscillation," AIAA Paper 2003-1731, April 2003.

[26]Snyder, R. D., Scott, J. N., Khot, N. S., Beran, P. S., and Zweber, J. V., "Predictions of Store-Induced Limit-Cycle Oscillations Using Euler and Navier–Stokes Fluid Dynamics," AIAA Paper 2003-1727, April 2003.